Check for updates

ENGINEERING

Magnetically gated millimeter-scale capsule power system for leadless electrotherapy

Feiyao Yang[1]†, Yu Tian[2]†, Enyi Zhang[3]†, Lixue Yang[1,4], Ziyue You[5], Puguang Peng[1,6], Han Qian[1,6], Yan Du[1,6], Haiwei Li[2], Yongquan Wu[2], Houfang Liu[3], Anfu Zhou[5], Tian-Ling Ren[3]*, Weiping Sun[2]*, Zhong Lin Wang[1]*, Di Wei[1,7]*

Copyright © 2026 The Authors, some rights reserved; exclusive licensee American Association for the Advancement of Science. No claim to original U.S. Government Works. Distributed under a Creative Commons Attribution NonCommercial License 4.0 (CC BY-NC).

Temporary cardiac pacing is indispensable for bridging transient bradyarrhythmic indications over days to weeks, yet existing systems remain constrained by device dimensions, surgical complexity, patient burden, and intrinsic operational principles. Here, these challenges are addressed through a millimeter-scale capsule power system with magnetically gated activation via a reed switch, which eliminates the stringent orientation and implantation-depth requirements of optically controlled approaches. In contrast to conventional reed switch-based pacemakers, this capsule system extends the functionality of the reed switch by integrating electrode materials directly onto its surface, thereby enabling a monolithic miniaturized architecture. Pulsed magnetic fields wirelessly actuate intermittent switching, enabling controlled discharge, with robust cardiac pacing demonstrated in large animals. A proof-of-concept closed-loop system is further realized, establishing the feasibility of future integration with a wearable electronic module to enable autonomous electrotherapy upon arrhythmia detection. Collectively, this strategy addresses a key limitation in temporary pacing and may provide a versatile framework for the development of temporary electrotherapeutic systems across cardiac, neural, and regenerative applications.

INTRODUCTION

Temporary cardiac pacing devices are indispensable for transient indications expected to last days to weeks (*1*). These devices provide demand-based atrial and/or ventricular stimulation, serving either as a bridge to permanent implantation (*2*) or as life-saving interventions for patients with short-lived bradyarrhythmias, such as those occurring after cardiac surgery, a heart attack or a medication overdose (*3*–*7*). Even when infrequent, device-related infections can be catastrophic, involving the generator pocket, leads, or both (*8*–*15*). Moreover, the externalized system is prone to inadvertent dislodgement during patient care (*6*), and lead removal can cause myocardial laceration or perforation due to fibrotic encapsulation of the electrode tip (*16*, *17*). Specific to transvenous pacing, endovascular surgeries are challenging for adult patients with contraindications to transvenous pacemakers and for infants and children with small body sizes and rapid patterns of growth, who undergo far more invasive epicardial approaches with the morbidities of thoracotomy (*18*–*21*). Commercial leadless pacemakers have been developed specifically to mitigate the complications associated with pacing leads, and delivered via a minimally invasive procedure to the right ventricle (*22*–*24*). However, their broader clinical translation is constrained by device dimensions, implantation demands and the integrated battery, alongside risks of myocardial perforation and device dislodgement (*23*, *24*). Furthermore, a battery-powered micropacemaker has been developed, offering particular advantages for patients with limited vascular access, young children and individuals with congenital heart disease who require epicardial access (*18*). Although energy-storage technologies have advanced substantially (*25*), batteries remain a major barrier to device miniaturization and functional expansion without increasing the implant burden (*26*, *27*).

To overcome these constraints, battery-free approaches based on wireless power transfer (*4*, *28*, *29*) and energy harvesting (*30*–*40*) have been actively explored. Wireless power transfer offers an alternative, yet many existing systems for epicardial pacing necessitate invasive open-chest implantation (thoracotomy), substantially increasing patient burden and recovery time (*17*, *41*–*44*). Moreover, a major technological challenge lies in the miniaturization of implantable receivers capable of efficient operation in deep tissue (*29*, *45*–*50*), while simultaneously maintaining compliance with regulatory power-exposure limits for general safety (*51*). On the other hand, energy-harvesting strategies are commonly constrained by challenges in device miniaturization, insufficient power density, reliable fixation within dynamic biological tissues and long-term biosafety, leaving most self-powered concepts at an investigational stage (*30*, *36*, *41*, *45*, *52*). For example, photovoltaic-based leadless stimulation (*34*, *53*, *54*) encompasses approaches such as pulsed infrared lasers, which are limited by high power requirements and strong water absorption (*55*–*58*), as well as optogenetic strategies that are intrinsically constrained by the need for genetic manipulation, thereby restricting their translational potential (*59*). Furthermore, optical control necessitates precise orientation of the phototransistor toward the body surface during implantation, while postoperative motion may induce device rotation or displacement, compromising optical coupling. In addition, performance is strongly constrained by implantation depth and by maximum permissible skin exposure limits imposed for safety (*60*, *61*). Although an improved design that positions the phototransistor closer to the skin while retaining intramyocardial pacing electrodes enables deeper-site stimulation (*7*), this configuration necessarily

[1]Beijing Institute of Nanoenergy and Nanosystems, Chinese Academy of Sciences, Beijing, P. R. China, 101400. [2]Cardiac Pacing and CIED Center, Beijing Anzhen Hospital. Capital Medical University, Beijing, P. R. China, 100029. [3]School of Integrated Circuits and Beijing National Research Center for Information Science and Technology (BNRist), Tsinghua University, Beijing, P. R. China, 100084. [4]School of Chemistry and Life Sciences, Changchun University of Technology, Changchun, P. R. China, 130012. [5]Beijing University of Posts and Telecommunications, Beijing, P. R. China, 100876. [6]School of Nanoscience and Engineering, University of Chinese Academy of Sciences, Beijing, P. R. China, 100049. [7]Centre for Photonic Devices and Sensors, University of Cambridge, 9 JJ Thomson Avenue, Cambridge, UK, CB3 0FA.
*Corresponding author. Email: rentl@tsinghua.edu.cn (T.-L.R.); 18611312085@163.com (W.S.); zlwang@binn.cas.cn (Z.L.W.); weidi@binn.cas.cn (D.W.)
†These authors contributed equally to this work.

Downloaded from https://www.science.org on October 16, 2026

increases device dimensions, complicating implantation and precluding minimally invasive delivery. Despite leadless pacemakers have achieved remarkable progress, their clinical translation remains constrained by device dimensions, surgical complexity, patient burden, and intrinsic operational principles (*3*, *18*, *36*, *41*, *43*, *45*). Especially, the implantation of pacemakers in neonates and infants requires particular consideration of small body size, marked body growth potential, and the decades of future pacing therapy to be expected (*20*). Consequently, the development of leadless pacemakers that can be implanted through minimally invasive procedures remains an important challenge in biomedical engineering.

In contrast to electromagnetic waves employed in wireless power transfer, which are readily absorbed by biological tissues, magnetic fields traverse such media with minimal attenuation, effectively analogous to propagation in free space (*28*, *43*, *62*), and are comparatively insensitive to the dynamic perturbations induced by cardiac motion. Here, an alternative strategy is introduced that exploits the depth-insensitive nature of magnetic control. Inspired by the capsule-like geometry of commercial leadless pacemakers while remaining compatible with established transvenous and minimally invasive implantation workflows (*22*–*24*), a millimeter-scale capsule power system actuated by a magnetic reed switch was developed (Fig. 1A, fig. S1, and table S1). Compared with previously reported conventional reed switch-based pacemakers (*36*, *63*, *64*), the present system incorporates several key conceptual and engineering advances (figs. S2 and S3 and text S1). The capsule power system weighs approximately 43.18 mg (fig. S4) and has dimensions of approximately φ1.8 mm × 5 mm, making it smaller than a grain of barley (Fig. 1B). Its dimensions are below those of the most compact capsule-shaped pacemakers reported to date, with a mass nearly half that of the lightest counterpart (*45*), and comparable in scale to the smallest planar architectures previously reported (*7*) (table S2). In contrast to planar designs, the capsule configuration offers a compact form factor that accommodates insertion through small-diameter (~2.67 mm) introducers (Fig. 1C; 8 Fr (French gauge)) and is inherently compatible with sheath-assisted, minimally invasive percutaneous injection and endovascular delivery (Fig. 1D). Given the subminiature size and ultralight weight of the capsule power system, it is amenable to minimally invasive implantation analogous to previously reported microscale device (*7*), thereby reducing device burden and procedural risk, and enabling applicability even in neonates. Experimental investigations elucidate the working mechanism, with robust cardiac pacing demonstrated in large animals (beagle dogs and Bama pig). A proof-of-concept closed-loop system is developed and validated in vivo in a beagle dog, demonstrating the feasibility of future integration with a skin-interfaced wearable electronic module for electrocardiogram (ECG) acquisition, signal processing, and magnetic-field actuation to enable autonomous electrotherapy upon arrhythmia detection.

RESULTS

Working mechanism

The capsule power system shown in this work exploits a self-powered mechanism, where the battery electrodes are the pacing electrodes. Specifically, an active zinc (Zn)-based composite serves as the anode, and a molybdenum trioxide (MoO_3) composite serves as the cathode (text S2 and table S3) (*65*, *66*). The cardiac tissue and associated biofluids act as the electrolyte to form a galvanic cell (Zn-MoO_3).

Downloaded from https://www.science.org on October 16, 2026

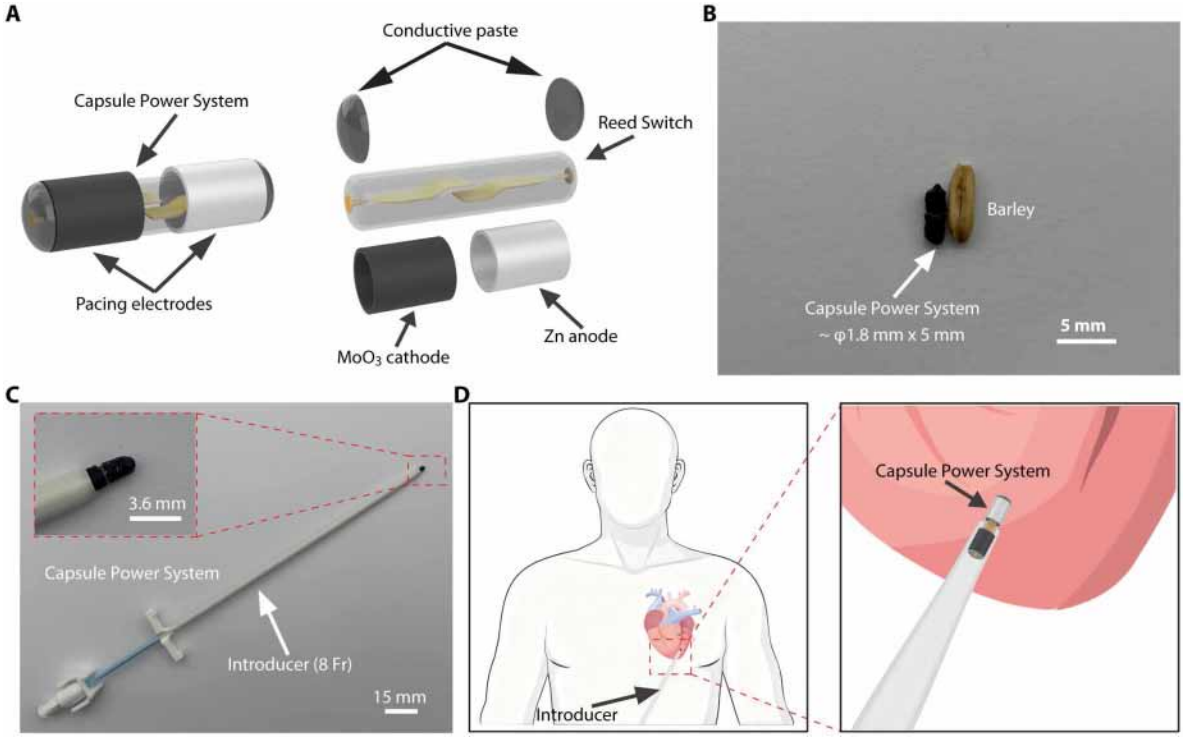


Fig. 1. Design of the capsule power system. (**A**) Schematic illustration of the system (left) and corresponding exploded view (right). (**B**) Photograph of the system, smaller than a grain of barley. (**C**) Photograph demonstrating accommodation of the system within an 8 Fr introducer. (**D**) Schematic illustrations of catheter-based implantation via injection.

The two electrodes are electrically connected through a reed switch that is actuated by a tissue-penetrating pulsed magnetic field. This component provides a magnetic principle to control the operation of the capsule power system with an external control module (fig. S5). In particular, the anode and cathode were respectively connected to the two terminals of the reed switch using a conductive paste. The conductive paste was prepared by incorporating tungsten (W) microparticles (fig. S6) into candelilla wax through a simple mixing process (*67*). Figure S7A shows a representative scanning electron microscopy (SEM) image of the conductive paste, while fig. S7B presents the corresponding energy-dispersive spectroscopy (EDS) elemental mapping, with red and green regions indicating W and wax, respectively. Figure S7C illustrates how the electrical conductivity of the conductive paste varies with the candelilla wax-to-W weight ratio. The entire structure, except for the interelectrode gap between the anode and cathode, is exposed at the interface with the cardiac tissue. Here, pacing is realized via transcutaneous transmission of pulsed magnetic fields, which wirelessly and on demand actuate intermittent switching of the capsule power system, thereby enabling pulsed discharge (fig. S3). During magnetic-field-free intervals, the device remains inactive, as the open reed switch interrupts current flow. Upon magnetic field application, the reed switch closes the circuit, permitting the galvanic cell discharge through the pacing electrodes into the adjacent cardiac tissue. The materials, structural components, and electrochemical operating principles of the galvanic cell collectively underpin the pacing mechanism.

With respect to the electrode-material selection (text S2), the corrosion kinetics of Zn lie between those of magnesium (Mg) and iron (Fe) (*68*), closely matching the timescales of vascular and soft-tissue healing, while its degradation products (Zn^{2+}) are physiologically essential and readily metabolized (*69*). Moreover, Zn anodes demonstrate superior electrochemical stability compared with Mg (*7*, *70*). Accordingly, both Zn foil and Zn-based composite anodes are theoretically well suited for this device. The Zn-based composite, consisting of Zn powder, conductive carbon black and poly(D,L-lactide-co-glycolide) (PLGA), was coated onto a Zn foil current collector to serve as the anode. MoO_3 has been extensively investigated as cathode material, as its higher electrochemical potential overcomes the voltage and energy-density limitations of metallic molybdenum (Mo) by exploiting ion-intercalation capability (*66*, *71*). A simple fabrication strategy, based on dispersing MoO_3 powder with a PLGA matrix, yields a percolating three-dimensional (3D) MoO_3 network while preserving electrolyte permeability. This architecture effectively increases the electrochemically active surface area, thereby simultaneously enhancing output voltage and achievable current capability (*66*). The enhanced output voltage is attributed to the reduction of Mo(VI) species at the cathode, combined with the 3D network architecture (*4*). The MoO_3 composite, consisting of MoO_3 nanopowder, conductive carbon black and PLGA, was coated onto a Mo current collector (Mo gauze or Mo foil) to form the cathode.

To verify the working mechanism and optimize the performance of the capsule power system, the planar device was designed and measured as shown in fig. S8. The commercial acrylic plate (0.6 mm thickness) was patterned into the device substrate using a computer-controlled CO_2 laser cutter. The resulting substrate measured 5 mm × 10 mm, with a 1 mm gap between the cathode and anode. The electrode materials were cut to the desired dimensions and assembled onto an acrylic substrate together with test wires using the conductive paste, forming a planar device (fig. S8A). Upon contact of the anode and cathode with cardiac tissue or an electrolyte, the anode underwent oxidation ($Zn - 2e^- \rightarrow Zn^{2+}$), while the cathode underwent reduction ($MoO_3 + ne^- \rightarrow MoO_3{}^{n-}$). As shown in fig. S8B, compared with the planar device employing a Zn foil anode, the device incorporating a Zn-based composite anode exhibited a higher and more stable output voltage, together with an increased short-circuit current (I_{sc}), in phosphate-buffered saline (PBS; pH 7.2–7.4, 0.01 M). During constant-current discharge at 0.3 mA in PBS, the Zn foil anode exhibited intense and rapid hydrogen (H_2) evolution within a short time (fig. S8C and movie S1), which could potentially damage myocardial tissue. By contrast, the Zn-based composite anode, in which Zn nanoparticles were encapsulated within a PLGA polymer matrix (fig. S8D), exhibited a moderated electrochemical reaction with negligible gas evolution (fig. S8C and movie S1). Encapsulation of Zn nanoparticles within the PLGA matrix enabled controlled Zn^{2+} release, thereby mitigating excessive ion accumulation associated with self-discharge or active discharge and maintaining Zn^{2+} concentrations within physiologically tolerable ranges. Morphological analysis revealed that the Zn foil anode exhibited a smooth and uniform surface before discharge (fig. S9A), whereas extensive corrosion and pore formation were observed after discharge (fig. S9B). The discharged surface was further covered with granular oxide deposits, which hindered electron transfer and contributed to voltage decay and performance degradation. In contrast, the Zn-based composite anode exhibited a smooth surface morphology prior to discharge (fig. S9C). Upon discharge, electrochemical reactions were largely confined to Zn nanoparticles exposed at the surface, whereas the underlying Zn nanoparticles remained encapsulated within the PLGA matrix and were uniformly distributed without evident oxide deposition (fig. S9D). This hierarchical structure enabled a continuous supply of electrochemically active Zn while minimizing surface passivation, thereby contributing to stable voltage output and sustained discharge performance. The morphological analysis, together with the electrochemical measurements (fig. S10, table S4, and text S3), consistently supports the conclusion that the Zn-based composite anode enhances interfacial charge transfer and mitigates voltage delay. Accordingly, compared with pure Zn foil, the Zn-based composite is more suitable as the anode material for the device. Unless otherwise specified, all devices described herein employ the Zn-based composite anode. The planar device incorporating the Zn-based composite anode exhibited an open-circuit voltage of approximately 0.90 V in PBS, consistent with previous reports (*65*), with a I_{sc} approaching 4.3 mA (fig. S8B). Notably, the device supported stable constant-current discharge at 0.5 mA (fig. S11A), fully satisfying the electrical requirements for cardiac pacing (*7*). As described above, during discharge the anode underwent oxidation ($Zn - 2e^- \rightarrow Zn^{2+}$), while the cathode experienced reduction ($MoO_3 + ne^- \rightarrow MoO_3{}^{n-}$), as confirmed by cyclic voltammetry (fig. S11B). Two distinct reduction peaks appeared within the potential range of 0.7–0.9 V, corresponding to the stepwise reduction of Mo^{6+} to lower valence states (for example, Mo^{5+} and Mo^{4+}), accompanied by intercalation of Zn^{2+} and/or H^+ ions into the MoO_3 layers. A pronounced oxidation peak at 1.1–1.2 V was attributed to reoxidation of reduced Mo species to Mo^{6+} and the concurrent deintercalation of Zn^{2+} and/or H^+ ions. These electrochemical features confirm the redox mechanisms governing device operation.

Performance and operational lifetime

To evaluate the potential of the planar device as a cardiac pacemaker, it was embedded within chicken tissue and connected in series

Downloaded from https://www.science.org on October 16, 2026

with a reed switch and a current measurement module to quantify the pulsed output current. A commercial microcontroller generated pulse signals to control relay switching at predefined frequencies and pulse widths, thereby regulating the on-off operation of the electromagnet circuit and producing pulsed magnetic fields that actuated the reed switch, resulting in pulsed discharge of the device. As shown in fig. S12, the device delivered pulsed discharge currents of at least 0.81 mA across multiple stimulation frequencies (60, 100 and 150 bpm) and pulse widths (5, 10, 20, 50 and 100 ms) in chicken tissue. Moreover, the dependence of the minimum pulsed current on pulse width at stimulation frequencies of 60, 100, and 150 bpm further confirms stable and reliable device performance (fig. S12, B, D, and F). If the minimum pulsed current exceeds the cardiac pacing threshold, reliable pacing can be achieved. Conversely, if it falls below this threshold, the device may fail to induce pacing or result in intermittent capture. Therefore, the minimum pulsed current constitutes a direct and critical determinant of effective cardiac pacing.

Despite the planar device exhibiting sufficient performance for temporary cardiac pacing (*7*), its geometry is poorly suited to introducers with circular inner diameters used for direct injection into the superficial subepicardial layer of the myocardium through small skin incisions. Moreover, the planar configuration intrinsically constrains energy density. By adopting a capsule-shaped design based on the reed switch-integrated architecture (Fig. 1A), these limitations are effectively overcome. Relative to the planar geometry, the capsule-shaped configuration is inherently compatible with sheath-assisted, minimally invasive percutaneous injection and endovascular delivery. Furthermore, for identical overall dimensions and electrode material compositions, the capsule-shaped structure affords a larger effective surface area, enabling greater electrode loading and consequently a higher energy density.

For electrochemical characterization, the capsule-shaped device was fabricated with test wires at both ends (Fig. 2A), distinct from the fully integrated configuration shown in Fig. 1A. The capsule-shaped device exhibited stable constant-current discharge at 0.5 mA in PBS (Fig. 2B), delivering a I_{sc} of approximately 3 mA and sustaining an open-circuit voltage (V_{oc}) of ~0.90 V (Fig. 2C). Using the same protocol as that employed for the planar device, the capsule-shaped device was embedded within chicken tissue to evaluate pulsed output performance. The device generated pulsed discharge currents of at least 0.96 mA across stimulation frequencies of 60, 100, and 150 bpm and pulse widths of 5, 10, 20, 50, and 100 ms (Fig. 2D and figs. S13 and S14), corresponding to an estimated pacing current density of approximately 4.25 mA cm^{-2}. Stable post-implantation performance was further corroborated by the dependence of the minimum pulsed current on pulse width at each stimulation frequency (fig. S14, B, D, and F). The minimum pulsed current consistently exceeds the cardiac pacing threshold (*7*), demonstrating that the device is fully capable of eliciting reliable cardiac pacing.

The total discharge capacity of the capsule-shaped device was approximately 0.67 mAh under continuous constant-current discharge at 0.5 mA (fig. S15). Under the pacing condition used in this study (0.5 mA, 60 bpm, 5 ms pulse width, corresponding to a duty cycle of 0.5%) (*7*), the theoretical operational lifetime under continuous pacing was estimated to be approximately 268 h (about 11 days). To evaluate the operational lifetime of the capsule-shaped device, agarose gel was employed as a surrogate for chicken tissue, owing to the rapid decomposition of the latter at ambient conditions. The impedance of chicken tissue is ~500 ohm at 1 kHz, corresponding to a pulse width of ~1 ms during cardiac pacing (*7*). The impedance of the agarose gel was tuned to match that of chicken tissue (fig. S16), allowing it to function as a phantom tissue for physiological impedance simulation (Fig. 2E and figs. S17 and S18). The capsule-shaped device was embedded in the agarose gel at 37°C to evaluate its operational lifetime. The pulsed discharge profiles demonstrate stable pulsed output for at least 30 days at a pacing rate of 60 bpm and a pulse width of 5 ms, with the minimum pulse current consistently maintained within the 0.75–1.02 mA range and showing no appreciable attenuation (Fig. 2F and text S4). Under these intermittent pulsed conditions (duty cycle 0.5%), the cumulative discharge time over 30 days is approximately 3.6 hours, which is consistent with the measured 0.67 mAh capacity. The off-intervals between pulses (99.5% of the total time) allow electrochemical recovery, including polarization relaxation and ion concentration gradient restoration, which effectively increases the usable capacity under pulsed operation relative to continuous-load measurement. These results, together with the previously reported 20-day in vivo pacing performance achieved using the same Zn-MoO_3 electrochemical system (*7*), suggest that the present device is capable of meeting the clinical requirements of temporary cardiac pacing, which has an average duration of approximately 4.2 days (*6*). The device is expected to remain stable under physiological cardiac motion because the rigid reed switch is mechanically robust and static magnetic fields propagate through biological tissues with negligible attenuation (*28*, *43*, *62*). In addition, the reed switch has a rated lifetime exceeding 10^7 switching cycles (table S1), far exceeding the ~3.63×10^5 cycles required for the average clinical duration of temporary cardiac pacing (4.2 days) (text S5). Future studies will focus on directly evaluating the in vivo operational lifetime and long-term pacing safety of the device in large animals.

Biological compatibility

Previous studies have demonstrated the biocompatibility of the conductive paste composed of candelilla wax and W, with no evidence of significant immune responses (*67*). PLGA is a US Food and Drug Administration (FDA)-approved, non-toxic polymer with well-documented biocompatibility (*72*, *73*). Other constituent materials, including Zn, W, Mo and MoO_3, generate primary degradation and electrochemical reaction products during pacing, predominantly $Zn(OH)_2$, H_2WO_4, and H_2MoO_4, respectively (table S5) (*4*, *65*), which are water-soluble and are harmlessly excreted via the renal pathway (*65*, *66*, *73*–*76*). In addition, H_2 generated as a secondary product during Zn degradation, analogous to that released during Mg corrosion, dissolves into surrounding tissues, diffuses through local tissue and vasculature, and can permeate through the skin (*77*).

In vitro cytocompatibility of the device was evaluated using mouse fibroblast cells via an indirect contact method (text S6). As shown in Fig. 3A, even at an extract concentration of 10%, the device group maintained cell viability comparable to that of the control group, with negligible adverse effects. To further evaluate biocompatibility, a four week in vivo assessment was conducted using twelve male Sprague Dawley rats (text S7). Animal body weights (Fig. 3B), routine haematological parameters, and serum biochemical indices (fig. S19, A and B) exhibited no statistically significant differences between the control and device groups, indicating favourable in vivo biocompatibility. At both 1 and 4 weeks after implantation, euthanized animals exhibited mild to moderate infiltration of inflammatory cells, including lymphocytes, at the implantation site. The extent of mixed epicardial inflammatory responses was comparable between the control

Downloaded from https://www.science.org on October 16, 2026

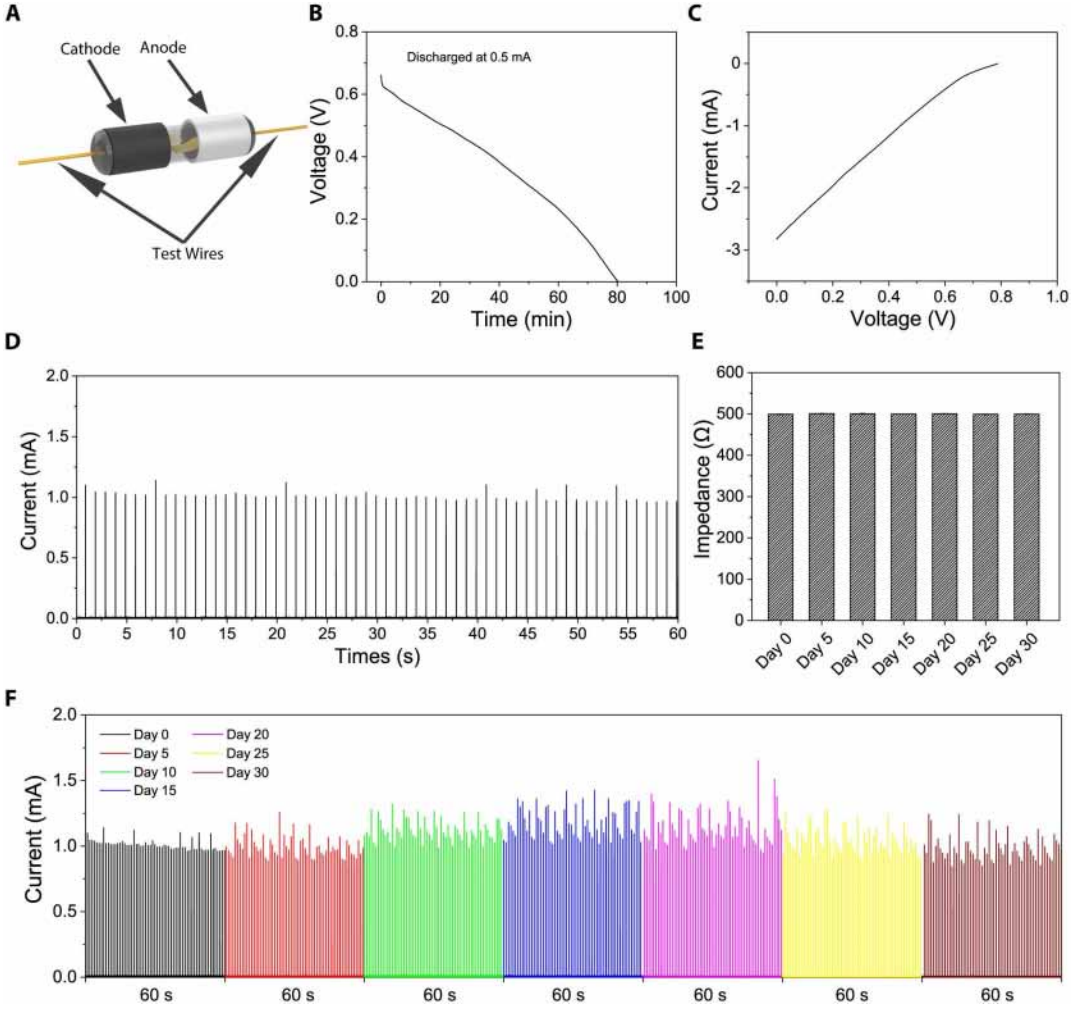


Fig. 2. Electrochemical characterization of the capsule-shaped device. (**A**) Device architecture with test wires connected at both ends. (**B**) Galvanostatic discharge profile recorded at 0.5 mA in phosphate-buffered saline (PBS; pH 7.2–7.4, 0.01 M) at 25°C and 80% relative humidity. (**C**) Current - voltage (I-V) characteristics measured at a scan rate of 10 mV s^{-1} in PBS (pH 7.2–7.4, 0.01 M) at 25°C and 80% relative humidity. (**D**) Output currents of the device under pulsed magnetic-field actuation in chicken tissue at 37 °C and 80% relative humidity. (**E**) Impedance magnitude of agarose gel measured at 1 kHz under physiological conditions (37 °C, 80% relative humidity). Data are presented as mean ± s.d., with error bars representing standard deviations from three independent measurements. Repeated- measures ANOVA, $P = 0.082$. (**F**) Pulsed output current of the device over time under pulsed magnetic-field actuation in agarose gel at 37°C and 80% relative humidity. Pulsed discharge was triggered at 60 bpm with a 5 ms pulse width (duty cycle 0.5%), and the output current was recorded daily. The cumulative discharge time over 30 days is approximately 3.6 hours.

and device groups (fig. S19, C to F). Collectively, these results, together with additional analyses (text S8), indicate that all constituent materials, including the electrodes, conductive additives, glass-based reed switch and the conductive pastes (*67*), are biocompatible. Moreover, compatibility with computed tomography (CT) imaging (fig. S20 and text S9) provides additional advantages for patients requiring routine medical imaging.

Feasibility of the pulsed magnetic fields

As shown in Fig. 1A, the cathode and anode of the capsule-shaped device cylindrically enclose the reed switch, leaving only the inter-electrode gap directly exposed to the pulsed magnetic field. During device activation for pacing, the pulsed magnetic field may induce a Faraday cage-like effect in the cylindrical metallic current collectors of the electrodes, thereby attenuating the magnetic field experienced by the reed switch. To assess the feasibility of magnetic actuation under these conditions, magnetic shielding simulations were performed to evaluate the magnetically controlled effectiveness of the device (text S10 and figs. S21 and S22). Given that the relative magnetic permeability of both biological tissues and air is approximately unity, the cylindrical metallic current collectors were embedded within a sufficiently large air domain for simulation. Under low-frequency magnetic fields (<10 kHz), the Mo and Zn cylinders provide virtually no shielding at the centre of the gap (Fig. 3, C to E, and fig. S23), and no appreciable eddy currents are generated across the cylinder cross-sections at 1 kHz (Fig. 3F and figs. S24 and S25). Although a Faraday cage-like effect can partially attenuate rapidly varying pulsed magnetic fields, cardiac pacing frequencies are intrinsically low (<10 Hz), rendering the shielding induced by 50 μm-thick cylindrical Mo and Zn current collectors effectively negligible. Consequently, the applied pulsed magnetic fields readily penetrate the metallic current collectors and reliably activate the capsule-shaped device for cardiac pacing.

Downloaded from https://www.science.org on October 16, 2026

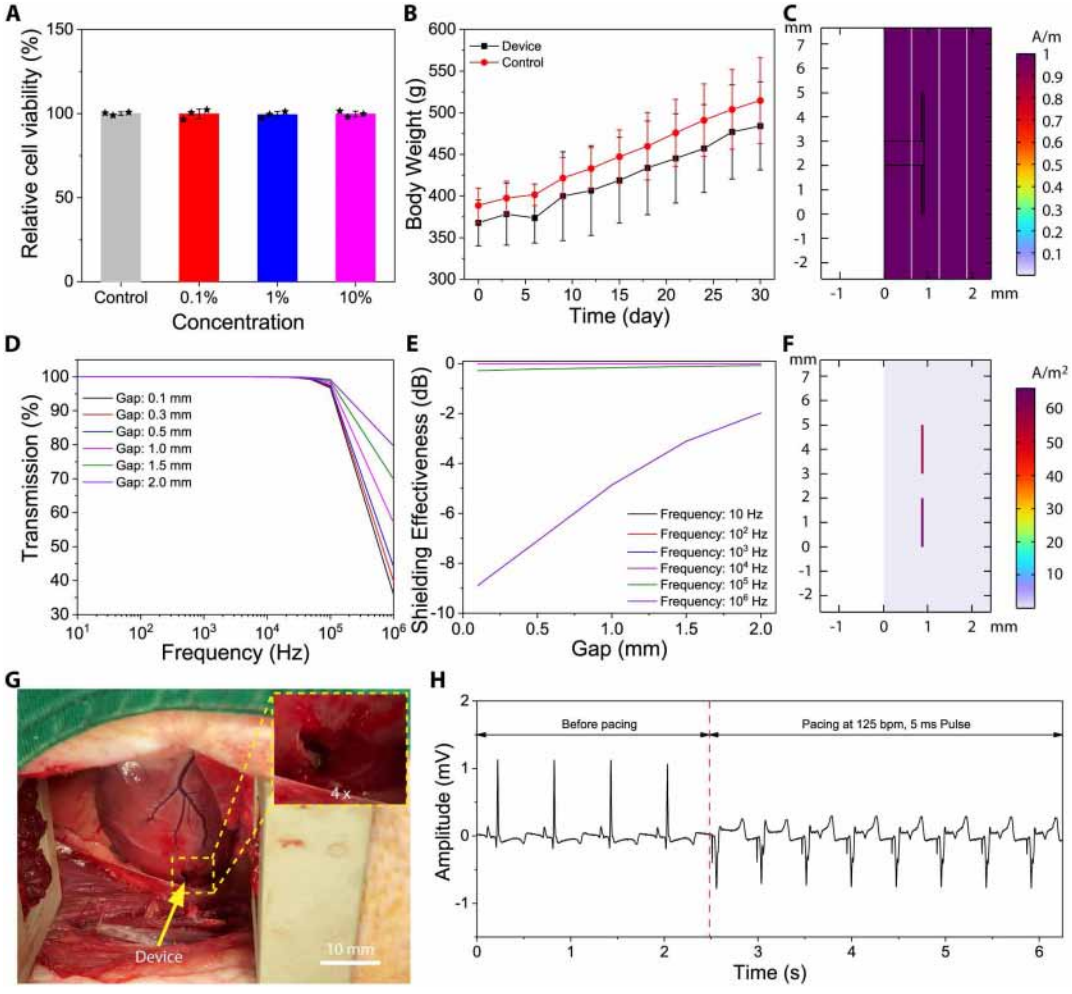


Fig. 3. Characterization of the capsule-shaped device. (**A**) Cell viability, expressed as the percentage of live cells, for the control group (no sample) and the device groups. Data are presented with error bars as mean ± s.d. $n = 3$ biological replicates. One-way ANOVA, $P = 0.981$. (**B**) Body weight trajectories of rats following implantation in the device and control groups. Data are presented with error bars as mean ± s.d. $n = 3$ biologically independent animals. Repeated Measures ANOVA, $P = 0.194$. (**C**) Spatial distributions of the magnetic field magnitude and magnetic flux lines at a pulsed magnetic field frequency of 1 kHz with an interelectrode gap of 1 mm. (**D**) Magnetic field transmittance as a function of frequency for different gap sizes. (**E**) Magnetic field shielding effectiveness as a function of gap size at different frequencies. (**F**) Cross-sectional distributions of eddy current density in the Mo and Zn cylinders at 1 kHz with an interelectrode gap of 1 mm. (**G**) Photograph of a porcine heart with the device embedded within the superficial subepicardial layers of the myocardium. Inset: a 4× magnified view. (**H**) Electrocardiographic (ECG) recordings obtained before and during cardiac pacing under pulsed magnetic field stimulation. The image (H) is intentionally reused with fig. S31A.

The commercial reed switch used in this study specifies a response time of 0.35 ms and a release time of 20 μs (table S1), both substantially shorter than the pacing pulse duration (5 ms) and interpulse interval (995 ms), thereby ensuring faithful transmission of the programmed pacing waveform. Consistent with this expectation, direct measurements showed that the electrical output pulses closely followed the applied magnetic-field pulses with a delay of approximately 0.41 ms (fig. S26), far beyond the requirements for cardiac pacing (text S11) (*78*). As discussed earlier, biological tissues exhibit magnetic susceptibilities close to that of vacuum, static magnetic fields are expected to penetrate tissue with negligible attenuation (*62*). Consistent with this prediction, ex vivo porcine tissue experiments showed that the magnetic-field strengths required for reed-switch activation through 10–50 mm-thick tissue closely matched those measured in air at the same distances (fig. S27, table S6, and text S12). Device activation was achieved with surface magnetic fields, confirming reliable magnetic actuation through biologically relevant tissue thicknesses.

In vivo pacing

In vivo pacing studies in clinically relevant large animals (beagle dog and Bama pig) demonstrated the functionality of devices implanted into the superficial subepicardial layers of the myocardium (text S13). Owing to its close similarity to the human heart in morphology, size and electrophysiological properties, the canine heart is widely used in cardiovascular research. The beagle dog, approved by international regulatory authorities including the US FDA and China's National Medical Products Administration (NMPA), serves as a standard preclinical animal. Accordingly, the beagle dog was selected for in vivo evaluation (fig. S28A). The open-thoracotomy implantation procedure and corresponding intraoperative images are presented in fig. S28, B to G. Placement of an electromagnet on the skin surface at the

Downloaded from https://www.science.org on October 16, 2026

left fourth to sixth intercostal spaces (fig. S29), followed by pulsed magnetic activation, successfully paced the canine heart at 150 bpm. Figure S30 presents ECG recordings obtained from the left ventricle under intrinsic rhythm and during pacing, demonstrating stable 1:1 capture across multiple pacing conditions with pulse widths of 5, 10, 50, and 100 ms, thereby confirming complete cardiac capture. Although effective cardiac pacing and capture were achieved in the beagle dog, additional validation was performed in the Bama pig to account for interspecies differences in cardiac physiology (fig. S31A). The Bama pig, a miniature breed developed in China, exhibits cardiac anatomy and cardiovascular physiology highly analogous to those of humans and is widely regarded as the gold-standard preclinical model for pacemakers and other cardiovascular devices. Using the same open-thoracotomy procedure, the device was implanted into the superficial subepicardial layer of the left ventricular myocardium (Fig. 3G and fig. S31, B to E). Under pulsed magnetic fields generated by an external skin-mounted electromagnet, stable pacing at 125 bpm with consistent 1:1 capture was achieved across a range of pulse widths (fig. S32). ECG recordings (Fig. 3H) confirm efficient left ventricular pacing and robust 1:1 capture at 125 bpm. Successful pacing in the Bama pig satisfies the standard 1:1 device's criterion, representing the final preclinical milestone toward clinical translation. Given the close anatomical and physiological resemblance to humans, pacing data obtained from the Bama pig can be reliably extrapolated to human clinical trials, consistent with regulatory practice endorsed by the FDA and NMPA.

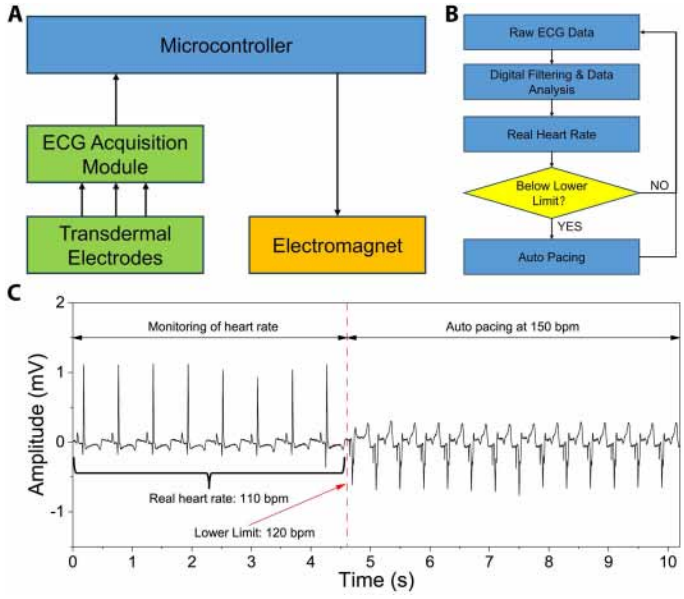


Fig. 4. Closed-loop cardiac electrotherapy. (**A**) System architecture of the proof-of-concept system. (**B**) Logical control flowchart of the proof-of-concept system. (**C**) ECG recordings demonstrating that detection of a heart rate below the bradycardia limit (120 bpm) automatically triggers pacing at 150 bpm with a pulse width of 5 ms.

Closed-loop cardiac electrotherapy

As described above, integration with a skin-interfaced wearable electronic module capable of ECG acquisition, signal analysis and programmed magnetic-field output enables autonomous, closed-loop cardiac electrotherapy upon arrhythmia detection. To validate closed-loop pacing, a proof-of-concept system is developed and evaluated in vivo in a beagle dog. The system comprises a commercial microcontroller, a commercial single-channel ECG acquisition module and a commercial electromagnet (Fig. 4A, fig. S33, and text S14). The ECG module employs medical-grade lead wires with surface limb electrodes (Ag/AgCl) configured in lead II and operated at a sampling rate of 1,000 Hz to acquire ECG signals in real time and transmit the processed data to the microcontroller. The microcontroller performs digital filtering, extracts real-time and averaged heart-rate features, and compares them against a predefined lower pacing limit. When the heart rate falls below this limit, the microcontroller generates pulse signals to modulate the switching of the electromagnet at specified frequencies and pulse widths, thereby producing pulsed magnetic fields to actuate the capsule-shaped device (Fig. 4B). The device was implanted into the superficial subepicardial layer of the left ventricular myocardium via lateral thoracotomy (fig. S28). As shown in Fig. 4C, detection of bradycardia, defined by a lower limit of 120 bpm, automatically triggered cardiac pacing at 150 bpm and achieved complete cardiac capture. Further development will be required to realize a fully integrated skin-interfaced wearable electronic module that combines ECG acquisition, signal processing and magnetic-field actuation, enabling autonomous electrotherapy upon arrhythmia detection.

DISCUSSION

In summary, we present a magnetically gated millimeter-scale capsule power system that enables wireless, on-demand activation of temporary cardiac pacing through externally applied pulsed magnetic fields. By directly integrating a microscale reed switch into the electrochemical architecture through conformal assembly of electrode materials, the device combines energy generation and magnetic switching within a single monolithic structure, thereby eliminating the need for onboard control circuitry and substantially reducing device dimensions. Unlike optically controlled approaches, which often require stringent alignment and implantation-depth constraints, magnetic activation provides robust wireless control independent of device orientation and tissue penetration depth. Furthermore, in contrast to conventional reed switch-based pacemakers, in which the reed switch serves primarily as a passive trigger for downstream electronic circuitry, the reed switch in the present system functions as an integrated component of the electrochemical energy-conversion architecture, representing a distinct design strategy for implantable electrotherapeutic systems. This architectural redefinition, transforming the reed switch from a passive magnetic trigger into an integrated electrochemical-structural component, while externalizing pacing control logic to programmable magnetic fields, represents a fundamental system-level shift, not a mere combination of off-the-shelf components. The resulting platform enables external regulation of pacing activation, frequency, and pulse width through programmable magnetic fields while maintaining an ultraminiaturized implanted architecture. Pulsed magnetic fields generated by an external control module actuate intermittent switching of the capsule power system, thereby enabling controllable pulsed discharge without embedded control electronics. This operating principle differs from previously reported leadless electrostimulators in terms of device architecture, energy-management strategy, and intended clinical implementation (table S2). Experimental studies elucidate the underlying working mechanism, optimize device performance, and identify a Zn-based composite as the preferred galvanic-cell anode.

Downloaded from https://www.science.org on October 16, 2026

Owing to its millimeter-scale dimensions and ultralight mass, the device is compatible with minimally invasive implantation strategies analogous to previously reported microscale implantable devices (*7*), potentially extending applicability to neonatal and pediatric patients. In addition, the capsule geometry is inherently compatible with sheath-assisted percutaneous injection, catheter-based deployment, and established transvenous workflows (*22*–*24*). Compatibility with clinical CT imaging further expands opportunities for image-guided implantation and future diagnotherapeutic applications (fig. S20 and text S9). Reliable pacing performance is demonstrated in both beagle dogs and Bama pigs using externally generated magnetic pulses, and a proof-of-concept closed-loop system integrating ECG acquisition, microcontroller-based feedback control, and wireless magnetic actuation is further validated in vivo in beagle dog.

Several challenges remain before clinical translation can be achieved. The present work represents a proof-of-concept demonstration, and future studies will require systematic evaluation of manufacturing reproducibility, batch-to-batch variability, and scalable automated fabrication processes. The current device architecture relies on a commercial reed switch that may undergo unintended activation under strong magnetic fields, including those generated during magnetic resonance imaging (MRI). Although MRI examinations are unlikely to be required during most temporary pacing procedures (*1*, *6*) and alternative imaging modalities such as CT and x-ray are often clinically available, the possibility of inadvertent MRI exposure cannot be completely excluded. In addition, the current system does not incorporate active voltage or current regulation circuitry, and the minimum achievable pulse width remains limited by the switching characteristics of the commercial mechanical relay. Independent amplitude control, which can be realized through electrode surface area design, multi-tap configurations, or calibrated external field strength, constitutes an engineering optimization fully compatible with the current architecture rather than a fundamental limitation of the proposed concept. Future device generations may benefit from biodegradable magnetically responsive variable-resistance technologies (*79*, *80*) with elevated magnetic-response thresholds, enabling both improved MRI compatibility and dynamic regulation of electrical outputs. Such developments may facilitate characterization of strength-duration relationships and determination of stimulation capture thresholds. In parallel, it is important to note that the mechanical relay resides exclusively in the external control module. Replacing it with a Metal-Oxide-Semiconductor Field Effect Transistor (MOSFET)-based electronic switching system, together with wearable miniaturized magnetic-pulse generation modules, would enable shorter stimulation pulses without any modification to the implanted capsule architecture, representing a near-term engineering upgrade that could reduce energy consumption and extend operational lifetimes while maintaining effective pacing performance.

The hybrid architecture was deliberately adopted: a hermetically sealed reed switch, selected for its reliability, mature fabrication, and clinical readiness, serves as a permanent micro-structural element analogous to clinically accepted passive implants, while all electrochemically active materials are rendered biodegradable to eliminate the need for device extraction. This design balances rapid clinical translation, enabled by commercially available components, with the long-term goal of minimizing residual implanted material, while anticipating future replacement of the reed switch by miniaturized or biodegradable alternatives. More broadly, this work establishes an alternative strategy for decoupling implanted therapeutic hardware from external control intelligence through magnetic-field-mediated energy switching. By relocating control functions outside the body while preserving a highly miniaturized implanted architecture, the proposed approach addresses longstanding challenges associated with device size, implantation complexity, and patient burden. Although further advances in device miniaturization, power management, magnetic-field control, and dry-electrode integration will be required, the overall system architecture remains inherently compatible with mature integrated-circuit design and microelectronic manufacturing technologies (text S15). Beyond temporary cardiac pacing, the underlying concept may be applicable to a broader range of electrotherapeutic systems, including cardiac, neural, and regenerative stimulation technologies, as well as other bioelectronic applications. Continued advances in materials, microelectronics, and wireless control technologies may ultimately facilitate the development of compact, wearable, and clinically translatable implantable medical systems.

MATERIALS AND METHODS

Preparation of the MoO_3 cathode

A slurry for the MoO_3 cathode was prepared by dispersing 30.8 wt% MoO_3 nanopowder (99.5% trace metals basis, ~100 nm, Sigma-Aldrich) and 3.4 wt% conductive carbon black (30–45 nm, XFNANO) in a PLGA (lactide:glycolide 65:35, molecular weight (M_w) 40,000 - 75,000, Sigma-Aldrich) solution (300 mg ml^{-1} in ethyl acetate, spectral grade, ≥99.5%, Macklin) under magnetic stirring (DLAB MS-H-Pro^A). Mo gauze (300 mesh, Xinwang Keyan) or Mo foil (50 μm thickness, Beijing Zhongke Yannuo New Materials) was used as the current collector. The slurry was coated onto one side of the collector and dried at 80°C for 1 h to complete cathode fabrication.

Preparation of the Zn-based composite anode

A slurry for the Zn-based composite anode was prepared by dispersing 33.3 wt% Zn powder (40–60 nm, Sigma-Aldrich) and 2.7 wt% conductive carbon black in PLGA solution (300 mg ml^{-1} in ethyl acetate) under magnetic stirring (DLAB MS-H-Pro^A). Zn foil (50 μm thickness, Beijing Zhongke Yannuo New Materials) was used as the current collector. The slurry was coated onto one side of the Zn foil and dried at 120°C for 50 min. The resulting Zn-based composite anodes were subsequently sintered in a 5 wt% acetic acid (99.5%, ACMEC) aqueous solution at room temperature for 30 min, followed by air drying.

Preparation of the conductive paste

The conductive paste was prepared following previous reported protocols (*67*). W powder (99.9% metals basis, 1–5 μm, Macklin) was mechanically mixed with candelilla wax (Macklin) at 120°C on a hotplate to obtain a homogeneous dispersion. The molten paste was drop-cast onto glass substrates through stencil masks to define well-controlled patterns, including circular features with a diameter of 26.5 mm for sheet-resistance measurements. Sheet resistance as a function of W loading was measured using a four - point probes resistivity measurement system (RTS-9, FOUR PROBES TECH). Sample thicknesses were determined by caliper measurements, allowing calculation of the corresponding electrical conductivities.

Preparation of the agarose gels

Agarose gels were prepared by dissolving 1 wt% agarose (low EEO, high EEO, M and biotechnology grades, Macklin), 0.0–0.9 wt% NaCl

Downloaded from https://www.science.org on October 16, 2026

(biotechnology grade, Macklin) and 0.5 wt% glycerol (99%, Macklin) in deionized (DI) water under magnetic stirring (DLAB MS-H-Pro^{A}) at 120°C to obtain a homogeneous solution. Upon cooling to room temperature, the solution solidified into an agarose gel. DI water with a resistivity exceeding 18 megohm cm^{-1} was obtained using a Milli-Q Biocel purification system.

Fabrication of the planar device

Commercial acrylic plates (0.6 mm thick) were patterned into device substrates using a computer-controlled CO_2 laser cutter (Speedy 300, Trotec). The resulting substrates (5 mm × 10 mm) were sequentially sonicated in ethanol (99.5%, Sigma-Aldrich) and DI water, and then dried. Both the Zn-based composite anode and the MoO_3 cathode were cut to the desired dimensions and, together with test wires, affixed onto the substrate using a conductive paste. This process yielded a planar device with a 1 mm interelectrode gap between the cathode and anode.

Fabrication of the capsule-shaped device with test wires

Commercial reed switches with conductive wires at both ends were sequentially ultrasonically cleaned in ethanol and DI water for 10 min each, followed by drying. The Zn-based composite anode and MoO_3 cathode were cut to the desired dimensions under an optical microscope using a surgical blade. The two electrodes were then attached onto the reed switch and electrically connected to the corresponding conductive wires at both ends using conductive paste. The assembly process was performed under microscopic assistance to ensure an interelectrode gap of approximately 1 mm between the cathode and anode. The resulting structure constituted the capsule-shaped device with external testing wires.

Fabrication of the capsule-shaped device

The original conductive wires at both ends of the commercial reed switch were first removed, after which the reed switch was sequentially ultrasonically cleaned in ethanol and DI water for 10 min each, followed by drying. Subsequently, the same assembly procedures used for the capsule-shaped device with testing wires were employed, including electrode cutting, conductive paste bonding, and interelectrode gap control under microscopic assistance. The final device exhibited overall dimensions of approximately φ1.8 mm × 5 mm, which were determined by the original dimensions of the reed switch.

Characterization and measurements

The device weight was measured using an electronic analytical balance (XSR105, METTLER TOLEDO). The morphologies of the anode materials, W powder and conductive paste were characterized by SEM (SU8020, Hitachi) operated at an accelerating voltage of 5.0 kV and an emission current of 10 μA, with EDS used for elemental analysis. Temperature and relative humidity (RH) were controlled using an environmental simulation test chamber (Votsch Technik). Device discharge behaviours were evaluated under constant-current discharge in PBS (pH 7.2–7.4, 0.01 M, cell culture grade, ACMEC). All electrochemical measurements were performed using an electrochemical workstation (Multi Autolab M204). Electrochemical impedance spectra (EIS) were recorded in potentiostatic mode over a frequency range of 10 kHz to 1 Hz with a voltage amplitude of 10 mV. To measure the pulsed output current of the device in tissue under a pulsed magnetic field, the device (embedded in chicken tissue), a reed switch and a current measurement module (National Instruments CompactDAQ 6218 BNC coupled with a Keithley 6514 electrometer) were electrically connected in series. An Arduino microcontroller generated pulse signals to control the switching of an electromagnet at defined frequencies and pulse widths, thereby producing pulsed magnetic fields to actuate the reed switch. Animal body weights were measured using an electronic balance (JCS-110001C, ZOGGI). Routine haematological and serum biochemical analyses were conducted using a haematology analyser (XN-1000 V-B1, Sysmex) and a clinical chemistry analyser (BS-420, Mindray), respectively. Representative images of haematoxylin and eosin (H&E)-stained cross-sections adjacent to the implantation site in control and device groups were acquired using a slide scanner (SQS-40P, TEKSQRAY). High-field medical imaging was conducted by CT (IMAGING 100, Raycision). The dedicated microcontroller-based testing platform employed an ESP32-C3 microcontroller unit (MCU), integrating an analog front-end and CPU system. The magnetic-field strength was measured using a Teslameter (DLX-STW1044, DELIXI).

Ethics statements

For in vivo biocompatibility of the device, all procedures were performed in accordance with the ethical standards and protocols of Beijing Anzhen Hospital. Capital Medical University (ethical approval number VS2126A00127). For in vivo demonstration of cardiac pacing in large animals, two male beagle dogs (8 months old, 11.8 kg & 11.6 kg, No. D25–002 & No. D26–023) and a female Bama pig (8 months old, 32.5 kg, No. D25–064) were maintained in accordance with the *Beijing Administrative Regulations on Laboratory Animals* (revised 2021), as approved by the Beijing Municipal Administrative Office of Laboratory Animals and issued by the Standing Committee of the Beijing Municipal People's Congress. The study protocol was approved by Beijing Anzhen Hospital, Capital Medical University (ethical approval numbers AE2025LLA019 and AE2026LLA012).

Supplementary Materials

The PDF file includes:

Supplementary Text S1 to S15
Figs. S1 to S33
Tables S1 to S6
Legend for movie S1
References

Other Supplementary Material for this manuscript includes the following:

Movie S1

REFERENCES

1. A. L. Waldo, J. L. Wells Jr., T. B. Cooper, W. A. H. MacLean, Temporary cardiac pacing: Applications and techniques in the treatment of cardiac arrhythmias. *Prog. Cardiovasc. Dis.* **23**, 451–474 (1981).
2. P. M. Zoll, R. H. Zoll, R. H. Falk, J. E. Clinton, D. R. Eitel, E. M. Antman, External noninvasive temporary cardiac pacing: Clinical trials. *Circulation* **71**, 937–944 (1985).
3. Y. S. Choi, R. T. Yin, A. Pfenniger, J. Koo, R. Avila, K. Benjamin Lee, S. W. Chen, G. Lee, G. Li, Y. Qiao, A. Murillo-Berlioz, A. Kiss, S. Han, S. M. Lee, C. Li, Z. Xie, Y.-Y. Chen, A. Burrell, B. Geist, H. Jeong, J. Kim, H.-J. Yoon, A. Banks, S.-K. Kang, Z. J. Zhang, C. R. Haney, A. V. Sahakian, D. Johnson, T. Efimova, Y. Huang, G. D. Trachiotis, B. P. Knight, R. K. Arora, I. R. Efimov, J. A. Rogers, Fully implantable and bioresorbable cardiac pacemakers without leads or batteries. *Nat. Biotechnol.* **39**, 1228–1238 (2021).
4. Y. Zhang, G. Lee, S. Li, Z. Hu, K. Zhao, J. A. Rogers, Advances in bioresorbable materials and electronics. *Chem. Rev.* **123**, 11722–11773 (2023).
5. Y. S. Choi, H. Jeong, R. T. Yin, R. Avila, A. Pfenniger, J. Yoo, J. Y. Lee, A. Tzavelis, Y. J. Lee, S. W. Chen, H. S. Knight, S. Kim, H.-Y. Ahn, G. Wickerson, A. Vázquez-Guardado, E. Higbee-Dempsey, B. A. Russo, M. A. Napolitano, T. J. Holleran, L. A. Razzak, A. N. Miniovich, G. Lee, B. Geist, B. Kim, S. Han, J. A. Brennan, K. Aras, S. S. Kwak, J. Kim, E. A. Waters, X. Yang, A. Burrell, K. San Chun, C. Liu, C. Wu, A. Y. Rwei, A. N. Spann, A. Banks,

Downloaded from https://www.science.org on October 16, 2026

D. Johnson, Z. J. Zhang, C. R. Haney, S. H. Jin, A. V. Sahakian, Y. Huang, G. D. Trachiotis, B. P. Knight, R. K. Arora, I. R. Efimov, J. A. Rogers, A transient, closed-loop network of wireless, body-integrated devices for autonomous electrotherapy. *Science* **376**, 1006–1012 (2022).
6. J. López Ayerbe, R. Villuendas Sabaté, C. García García, O. Rodríguez Leor, M. Gómez Pérez, A. Curós Abadal, J. Serra Flores, E. Larrousse, V. Valle, Temporary pacemakers: Current use and complications. *Rev. Esp. Cardiol. Engl. Ed.* **57**, 1045–1052 (2004).
7. Y. Zhang, E. Rytkin, L. Zeng, J. U. Kim, L. Tang, H. Zhang, A. Mikhailov, K. Zhao, Y. Wang, L. Ding, X. Lu, A. Lantsova, E. Aprea, G. Jiang, S. Li, S. G. Seo, T. Wang, J. Wang, J. Liu, J. Gu, F. Liu, K. Bailey, Y. F. L. Li, A. Burrell, A. Pfenniger, A. Ardashev, T. Yang, N. Liu, Z. Lv, N. S. Purwanto, Y. Ying, Y. Lu, C. Hoepfner, A. Melisova, J. Gong, J. Jeong, J. Choi, A. Hou, R. Nolander, W. Bai, S. H. Jin, Z. Ma, J. M. Torkelson, Y. Huang, W. Ouyang, R. K. Arora, I. R. Efimov, J. A. Rogers, Millimetre-scale bioresorbable optoelectronic systems for electrotherapy. *Nature* **640**, 77–86 (2025).
8. M. J. Wilhelm, C. Schmid, D. Hammel, S. Kerber, H. M. Loick, M. Herrmann, H. H. Scheld, Cardiac pacemaker infection: Surgical management with and without extracorporeal circulation. *Ann. Thorac. Surg.* **64**, 1707–1712 (1997).
9. F. J. Lumia, J. C. Rios, Temporary transvenous pacemaker therapy: An analysis of complications. *Chest* **64**, 604–608 (1973).
10. K. D. Donovan, K. Y. Lee, Indications for and complications of temporary transvenous cardiac pacing. *Anaesth. Intensive Care* **13**, 63–70 (1985).
11. M. U. Braun, T. Rauwolf, M. Bock, U. Kappert, A. Boscheri, A. Schnabel, R. H. Strasser, percutaneous lead implantation connected to an external device in stimulation-dependent patients with systemic infection—A prospective and controlled study. *Pacing Clin. Electrophysiol.* **29**, 875–879 (2006).
12. R. E. Kirkfeldt, J. B. Johansen, E. A. Nohr, O. D. Jørgensen, J. C. Nielsen, Complications after cardiac implantable electronic device implantations: An analysis of a complete, nationwide cohort in Denmark. *Eur. Heart J.* **35**, 1186–1194 (2013).
13. E. O. Udo, N. P. A. Zuithoff, N. M. van Hemel, C. C. de Cock, T. Hendriks, P. A. Doevendans, K. G. M. Moons, Incidence and predictors of short- and long-term complications in pacemaker therapy: The FOLLOWPACE study. *Heart Rhythm* **9**, 728–735 (2012).
14. M. Dębski, M. Ulman, A. Ząbek, K. Boczar, K. Haberka, M. Kuniewicz, J. Lelakowski, B. Małecka, Lead-related complications after DDD pacemaker implantation. *Kardiol. Pol.* **76**, 1224–1231 (2018).
15. R. G. Hauser, D. L. Hayes, L. M. Kallinen, D. S. Cannom, A. E. Epstein, A. K. Almquist, S. L. Song, G. F. O. Tyers, S. C. Vlay, M. Irwin, Clinical experience with pacemaker pulse generators and transvenous leads: An 8-year prospective multicenter study. *Heart Rhythm* **4**, 154–160 (2007).
16. E. Elmistekawy, Safety of temporary pacemaker wires. *Asian Cardiovasc. Thorac. Ann.* **27**, 341–346 (2019).
17. P. Gutruf, R. T. Yin, K. B. Lee, J. Ausra, J. A. Brennan, Y. Qiao, Z. Xie, R. Peralta, O. Talarico, A. Murillo, S. W. Chen, J. P. Leshock, C. R. Haney, E. A. Waters, C. Zhang, H. Luan, Y. Huang, G. Trachiotis, I. R. Efimov, J. A. Rogers, Wireless, battery-free, fully implantable multimodal and multisite pacemakers for applications in small animal models. *Nat. Commun.* **10**, 5742 (2019).
18. Y. Bar-Cohen, M. J. Silka, A. C. Hill, J. D. Pruetz, R. H. Chmait, L. Zhou, S. M. Rabin, V. Norekyan, G. E. Loeb, Minimally invasive implantation of a micropacemaker into the pericardial space. *Circ. Arrhythm. Electrophysiol.* **11**, e006307 (2018).
19. J. Zhao, Y. Huang, L. Lei, Z. Yao, T. Liu, H. Qiu, C. Lin, X. Liu, Y. Teng, X. Li, Y. Zhang, J. Zhuang, J. Chen, S. Wen, Permanent epicardial pacing in neonates and infants less than 1 year old: 12-year experience at a single center. *Transl. Pediatr.* **11**, 825–833 (2022).
20. M. Wildbolz, H. Dave, R. Weber, M. Gass, C. Balmer, Pacemaker implantation in neonates and infants: Favorable outcomes with epicardial pacing systems. *Pediatr. Cardiol.* **41**, 910–917 (2020).
21. M. I. Cohen, D. M. Bush, V. L. Vetter, R. E. Tanel, T. S. Wieand, J. W. Gaynor, L. A. Rhodes, Permanent epicardial pacing in pediatric patients. *Circulation* **103**, 2585–2590 (2001).
22. J. Z. Lee, S. K. Mulpuru, W. K. Shen, Leadless pacemaker: Performance and complications. *Trends Cardiovasc. Med.* **28**, 130–141 (2018).
23. V. Y. Reddy, D. V. Exner, D. J. Cantillon, R. Doshi, T. J. Bunch, G. F. Tomassoni, P. A. Friedman, N. A. M. Estes III, J. Ip, I. Niazi, K. Plunkitt, R. Banker, J. Porterfield, J. E. Ip, S. R. Dukkipati, LEADLESS II Study Investigators, Percutaneous implantation of an entirely intracardiac leadless pacemaker. *N. Engl. J. Med.* **373**, 1125–1135 (2015).
24. D. Reynolds, G. Z. Duray, R. Omar, K. Soejima, P. Neuzil, S. Zhang, C. Narasimhan, C. Steinwender, J. Brugada, M. Lloyd, P. R. Roberts, V. Sagi, J. Hummel, M. G. Bongiorni, R. E. Knops, C. R. Ellis, C. C. Gornick, M. A. Bernabei, V. Laager, K. Stromberg, E. R. Williams, J. H. Hudnall, P. Ritter, A leadless intracardiac transcatheter pacing system. *N. Engl. J. Med.* **374**, 533–541 (2016).
25. Z. Xiao, Z. Liu, X. Wu, X. Xiao, Y. Liu, J. Liu, Z. Zheng, W. Yao, J.-C. Li, G. Zhou, Artificial protrusion architectures enabling horizontal-diffusion nucleation for stable zinc-based batteries. *J. Am. Chem. Soc.* **147**, 32216–32224 (2025).
26. G. Iddan, G. Meron, A. Glukhovsky, P. Swain, Wireless capsule endoscopy. *Nature* **405**, 417–417 (2000).
27. M. Armand, J. M. Tarascon, Building better batteries. *Nature* **451**, 652–657 (2008).
28. A. Kurs, A. Karalis, R. Moffatt, J. D. Joannopoulos, P. Fisher, M. Soljačić, Wireless power transfer via strongly coupled magnetic resonances. *Science* **317**, 83–86 (2007).
29. S. Kim, J. S. Ho, A. S. Y. Poon, Midfield wireless powering of subwavelength autonomous devices. *Phys. Rev. Lett.* **110**, 203905 (2013).
30. C. Dagdeviren, B. D. Yang, Y. Su, P. L. Tran, P. Joe, E. Anderson, J. Xia, V. Doraiswamy, B. Dehdashti, X. Feng, B. Lu, R. Poston, Z. Khalpey, R. Ghaffari, Y. Huang, M. J. Slepian, J. A. Rogers, Conformal piezoelectric energy harvesting and storage from motions of the heart, lung, and diaphragm. *Proc. Natl. Acad. Sci. U.S.A.* **111**, 1927–1932 (2014).
31. H. Ryu, H.-m. Park, M.-K. Kim, B. Kim, H. S. Myoung, T. Y. Kim, H.-J. Yoon, S. S. Kwak, J. Kim, T. H. Hwang, E.-K. Choi, S.-W. Kim, Self-rechargeable cardiac pacemaker system with triboelectric nanogenerators. *Nat. Commun.* **12**, 4374 (2021).
32. Q. Zheng, B. Shi, F. Fan, X. Wang, L. Yan, W. Yuan, S. Wang, H. Liu, Z. Li, Z. L. Wang, In vivo powering of pacemaker by breathing-driven implanted triboelectric nanogenerator. *Adv. Mater.* **26**, 5851–5856 (2014).
33. Q. Zheng, Q. Tang, Z. L. Wang, Z. Li, Self-powered cardiovascular electronic devices and systems. *Nat. Rev. Cardiol.* **18**, 7–21 (2021).
34. B. Shi, Z. Li, Y. Fan, Implantable energy-harvesting devices. *Adv. Mater.* **30**, 1801511 (2018).
35. N. Li, Z. Yi, Y. Ma, F. Xie, Y. Huang, Y. Tian, X. Dong, Y. Liu, X. Shao, Y. Li, L. Jin, J. Liu, Z. Xu, B. Yang, H. Zhang, Direct powering a real cardiac pacemaker by natural energy of a heartbeat. *ACS Nano* **13**, 2822–2830 (2019).
36. H. Ouyang, Z. Liu, N. Li, B. Shi, Y. Zou, F. Xie, Y. Ma, Z. Li, H. Li, Q. Zheng, X. Qu, Y. Fan, Z. L. Wang, H. Zhang, Z. Li, Symbiotic cardiac pacemaker. *Nat. Commun.* **10**, 1821 (2019).
37. K. Ni, R. Liu, Moisture-induced iontronics for self-powered electronics. *Iontronics* **2**, 7 (2026).
38. S. Ding, T. Saha, L. Yin, R. Liu, M. I. Khan, A.-Y. Chang, H. Lee, H. Zhao, Y. Liu, A. S. Nazemi, J. Zhou, C. Chen, Z. Li, C. Zhang, S. Earney, S. Tang, O. Djassemi, X. Chen, M. Lin, S. S. Sandhu, J.-M. Moon, C. Moonla, P. Nandhakumar, Y. Park, K. Mahato, S. Xu, J. Wang, A fingertip-wearable microgrid system for autonomous energy management and metabolic monitoring. *Nat. Electron.* **7**, 788–799 (2024).
39. W. Kwak, J. Yin, S. Wang, J. Chen, Advances in triboelectric nanogenerators for self-powered wearable respiratory monitoring. *FlexMat* **1**, 5–22 (2024).
40. D. Wei, Writable electrochemical energy source based on graphene oxide. *Sci. Rep.* **5**, 15173 (2015).
41. S. Wang, Q. Cui, P. Abiri, M. Roustaei, E. Zhu, Y.-R. Li, K. Wang, S. Duarte, L. Yang, R. Ebrahimi, M. Bersohn, J. Chen, T. K. Hsiai, A self-assembled implantable microtubular pacemaker for wireless cardiac electrotherapy. *Sci. Adv.* **9**, eadj0540 (2023).
42. R. T. Yin, S. W. Chen, K. Benjamin Lee, Y. S. Choi, J. Koo, Q. Yang, M. A. Napolitano, J. Ausra, T. J. Holleran, J. B. Lapiano, E. Alex Waters, A. Brikha, G. Kowalik, A. N. Miniovich, H. S. Knight, B. A. Russo, A. Kiss, A. Murillo-Berlioz, T. Efimova, C. R. Haney, P. Gutruf, J. A. Rogers, G. D. Trachiotis, I. R. Efimov, Open thoracic surgical implantation of cardiac pacemakers in rats. *Nat. Protoc.* **18**, 374–395 (2023).
43. H. Lyu, M. John, D. Burkland, B. Greet, A. Post, A. Babakhani, M. Razavi, Synchronized biventricular heart pacing in a closed-chest porcine model based on wirelessly powered leadless pacemakers. *Sci. Rep.* **10**, 2067 (2020).
44. M. S. Silvetti, F. Drago, D. Di Carlo, S. Placidi, G. Brancaccio, A. Carotti, Cardiac pacing in paediatric patients with congenital heart defects: Transvenous or epicardial? *Europace* **15**, 1280–1286 (2013).
45. J. S. Ho, A. J. Yeh, E. Neofytou, S. Kim, Y. Tanabe, B. Patlolla, R. E. Beygui, A. S. Y. Poon, Wireless power transfer to deep-tissue microimplants. *Proc. Natl. Acad. Sci. U.S.A.* **111**, 7974–7979 (2014).
46. K. Agarwal, R. Jegadeesan, Y. X. Guo, N. V. Thakor, Wireless power transfer strategies for implantable bioelectronics. *IEEE Rev. Biomed. Eng.* **10**, 136–161 (2017).
47. S. R. Khan, S. K. Pavuluri, G. Cummins, M. P. Y. Desmulliez, Wireless power transfer techniques for implantable medical devices: A review. *Sensors* **20**, 3487 (2020).
48. S. Kim, J. S. Ho, L. Y. Chen, A. S. Y. Poon, Wireless power transfer to a cardiac implant. *Appl. Phys. Lett.* **101**, 234107 (2012).
49. D. R. Agrawal, Y. Tanabe, D. Weng, A. Ma, S. Hsu, S.-Y. Liao, Z. Zhen, Z.-Y. Zhu, C. Sun, Z. Dong, F. Yang, H. F. Tse, A. S. Y. Poon, J. S. Ho, Conformal phased surfaces for wireless powering of bioelectronic microdevices. *Nat. Biomed. Eng.* **1**, 0043 (2017).
50. J. Kim, R. Ghaffari, D.-H. Kim, The quest for miniaturized soft bioelectronic devices. *Nat. Biomed. Eng.* **1**, 0049 (2017).
51. IEEE Standard for Safety Levels with Respect to Human Exposure to Radio Frequency Electromagnetic Fields, 3 kHz to 300 GHz. *IEEE Std C95.1–2005 (Revision of IEEE Std C95.1–1991)* (2006), pp. 1–238.
52. B. Lu, Y. Chen, D. Ou, H. Chen, L. Diao, W. Zhang, J. Zheng, W. Ma, L. Sun, X. Feng, Ultra-flexible piezoelectric devices integrated with heart to harvest the biomechanical energy. *Sci. Rep.* **5**, 16065 (2015).
53. A. Haeberlin, A. Zurbuchen, J. Schaerer, J. Wagner, S. Walpen, C. Huber, H. Haeberlin, J. Fuhrer, R. Vogel, Successful pacing using a batteryless sunlight-powered pacemaker. *Europace* **16**, 1534–1539 (2014).

Downloaded from https://www.science.org on October 16, 2026

54. Z. Liu, B. Wen, L. Cao, S. Zhang, Y. Lei, G. Zhao, L. Chen, J. Wang, Y. Shi, J. Xu, X. Pan, L. Yu, Photoelectric cardiac pacing by flexible and degradable amorphous Si radial junction stimulators. *Adv. Healthc. Mater.* **9**, e1901342 (2020).
55. M. W. Jenkins, A. R. Duke, S. Gu, Y. Doughman, H. J. Chiel, H. Fujioka, M. Watanabe, E. D. Jansen, A. M. Rollins, Optical pacing of the embryonic heart. *Nat. Photonics* **4**, 623–626 (2010).
56. M. W. Jenkins, Y. T. Wang, Y. Q. Doughman, M. Watanabe, Y. Cheng, A. M. Rollins, Optical pacing of the adult rabbit heart. *Biomed. Opt. Express* **4**, 1626–1635 (2013).
57. Y. Jiang, X. Li, B. Liu, J. Yi, Y. Fang, F. Shi, X. Gao, E. Sudzilovsky, R. Parameswaran, K. Koehler, V. Nair, J. Yue, K. Guo, Y. Fang, H.-M. Tsai, G. Freyermuth, R. C. S. Wong, C.-M. Kao, C.-T. Chen, A. W. Nicholls, X. Wu, G. M. G. Shepherd, B. Tian, Rational design of silicon structures for optically controlled multiscale biointerfaces. *Nat. Biomed. Eng.* **2**, 508–521 (2018).
58. A. Prominski, J. Shi, P. Li, J. Yue, Y. Lin, J. Park, B. Tian, M. Y. Rotenberg, Porosity-based heterojunctions enable leadless optoelectronic modulation of tissues. *Nat. Mater.* **21**, 647–655 (2022).
59. U. Nussinovitch, L. Gepstein, Optogenetics for in vivo cardiac pacing and resynchronization therapies. *Nat. Biotechnol.* **33**, 750–754 (2015).
60. R. Chen, F. Gore, Q.-A. Nguyen, C. Ramakrishnan, S. Patel, S. H. Kim, M. Raffiee, Y. S. Kim, B. Hsueh, E. Krook-Magnusson, I. Soltesz, K. Deisseroth, Deep brain optogenetics without intracranial surgery. *Nat. Biotechnol.* **39**, 161–164 (2021).
61. H. Chamkouri, Implantable light therapy devices: Exploring red and infrared light for spinal cord regeneration. *SmartSys* **1**, e70009 (2025).
62. J. F. Schenck, The role of magnetic susceptibility in magnetic resonance imaging: MRI magnetic compatibility of the first and second kinds. *Med. Phys.* **23**, 815–850 (1996).
63. J. I. Laughner, S. B. Marrus, E. R. Zellmer, C. J. Weinheimer, M. R. MacEwan, S. X. Cui, J. M. Nerbonne, I. R. Efimov, A fully implantable pacemaker for the Mouse: From battery to wireless power. *PLOS ONE* **8**, e76291 (2013).
64. Y. Zhang, T. Sun, X. Yang, L. Zhou, C. M. J. Tan, M. Lei, H. Bayley, A microscale soft lithium-ion battery for tissue stimulation. *Nat. Chem. Eng.* **1**, 691–701 (2024).
65. Y. Zhang, F. Liu, Y. Zhang, J. Wang, D. D'Andrea, J. B. Walters, S. Li, H.-J. Yoon, M. Wu, S. Li, Z. Hu, T. Wang, J. Choi, K. Bailey, E. Dempsey, K. Zhao, A. Lantsova, Y. Bouricha, I. Huang, H. Guo, X. Ni, Y. Wu, G. Lee, F. Jiang, Y. Huang, C. K. Franz, J. A. Rogers, Self-powered, light-controlled, bioresorbable platforms for programmed drug delivery. *Proc. Natl. Acad. Sci. U.S.A.* **120**, e2217734120 (2023).
66. X. Huang, D. Wang, Z. Yuan, W. Xie, Y. Wu, R. Li, Y. Zhao, D. Luo, L. Cen, B. Chen, H. Wu, H. Xu, X. Sheng, M. Zhang, L. Zhao, L. Yin, A fully biodegradable battery for self-powered transient implants. *Small* **14**, e1800994 (2018).
67. S. M. Won, J. Koo, K. E. Crawford, A. D. Mickle, Y. Xue, S. Min, L. A. McIlvried, Y. Yan, S. B. Kim, S. M. Lee, B. H. Kim, H. Jang, M. R. MacEwan, Y. Huang, R. W. Gereau IV, J. A. Rogers, Natural wax for transient electronics. *Adv. Funct. Mater.* **28**, 1801819 (2018).
68. P. K. Bowen, J. Drelich, J. Goldman, Zinc exhibits ideal physiological corrosion behavior for bioabsorbable stents. *Adv. Mater.* **25**, 2577–2582 (2013).
69. P. K. Bowen, R. J. Guillory II, E. R. Shearier, J.-M. Seitz, J. Drelich, M. Bocks, F. Zhao, J. Goldman, Metallic zinc exhibits optimal biocompatibility for bioabsorbable endovascular stents. *Mater. Sci. Eng. C* **56**, 467–472 (2015).
70. Z. Wang, Y. Zhang, B. Yang, W. Li, H. Zhu, X. Zeng, S. Liu, The road ahead for hydrogel electrolytes in aqueous zinc metal batteries. *Iontronics* **2**, 16 (2026).
71. I. A. de Castro, R. S. Datta, J. Z. Ou, A. Castellanos-Gomez, S. Sriram, T. Daeneke, K. Kalantar-zadeh, Molybdenum oxides – from fundamentals to functionality. *Adv. Mater.* **29**, 1701619 (2017).
72. S. Lee, J. Koo, S.-K. Kang, G. Park, Y. J. Lee, Y.-Y. Chen, S. A. Lim, K.-M. Lee, J. A. Rogers, Metal microparticle – Polymer composites as printable, bio/ecoresorbable conductive inks. *Mater. Today* **21**, 207–215 (2018).
73. Y. S. Choi, J. Koo, Y. J. Lee, G. Lee, R. Avila, H. Ying, J. Reeder, L. Hambitzer, K. Im, J. Kim, K.-M. Lee, J. Cheng, Y. Huang, S.-K. Kang, J. A. Rogers, Biodegradable polyanhydrides as encapsulation layers for transient electronics. *Adv. Funct. Mater.* **30**, 2000941 (2020).
74. L. Yin, H. Cheng, S. Mao, R. Haasch, Y. Liu, X. Xie, S.-W. Hwang, H. Jain, S.-K. Kang, Y. Su, R. Li, Y. Huang, J. A. Rogers, Dissolvable metals for transient electronics. *Adv. Funct. Mater.* **24**, 645–658 (2014).
75. G. Song, Control of biodegradation of biocompatable magnesium alloys. *Corros. Sci.* **49**, 1696–1701 (2007).
76. A. Schauer, C. Redlich, J. Scheibler, G. Poehle, P. Barthel, A. Maennel, V. Adams, T. Weissgaerber, A. Linke, P. Quadbeck, Biocompatibility and degradation behavior of molybdenum in an in vivo rat model. *Materials* **14**, 7776 (2021).
77. J. Kuhlmann, I. Bartsch, E. Willbold, S. Schuchardt, O. Holz, N. Hort, D. Höche, W. R. Heineman, F. Witte, Fast escape of hydrogen from gas cavities around corroding magnesium implants. *Acta Biomater.* **9**, 8714–8721 (2013).
78. M. K. Chung, A. Fagerlin, P. J. Wang, T. B. Ajayi, L. A. Allen, T. Baykaner, E. J. Benjamin, M. Branda, K. L. Cavanaugh, L. Y. Chen, G. H. Crossley, R. K. Delaney, L. L. Eckhardt, K. L. Grady, I. G. Hargraves, M. True Hills, M. M. Kalscheur, D. B. Kramer, M. Kunneman, R. Lampert, A. T. Langford, K. B. Lewis, Y. Lu, J. M. Mandrola, K. Martinez, D. D. Matlock, S. R. McCarthy, V. M. Montori, P. A. Noseworthy, K. M. Orland, E. Ozanne, R. Passman, K. Pundi, D. M. Roden, E. V. Saarel, M. M. Schmidt, S. F. Sears, D. Stacey, R. S. Stafford, B. A. Steinberg, S. Youn Wass, J. M. Wright, Shared decision making in cardiac electrophysiology procedures and arrhythmia management. *Circ. Arrhythm. Electrophysiol.* **14**, e007958 (2021).
79. I. Bica, Quadrupolar magnetoresistor based on electroconductive magnetorheological elastomer. *J. Ind. Eng. Chem.* **15**, 769–772 (2009).
80. A. K. Jena, A. K. Sahoo, J. Mohanty, Effects of magnetic field on resistive switching in multiferroic based Ag/$BiFeO_3$/FTO RRAM device. *Appl. Phys. Lett.* **116**, 092901 (2020).
81. Y. F. Zheng, X. N. Gu, F. Witte, Biodegradable metals. *Mater. Sci. Eng. R* **77**, 1–34 (2014).
82. J.-L. Wang, J.-K. Xu, C. Hopkins, D. H.-K. Chow, L. Qin, Biodegradable magnesium-based implants in orthopedics—A general review and perspectives. *Adv. Sci.* **7**, 1902443 (2020).
83. A. Gangan, M. ElSabbagh, M. A. Bedair, H. M. Ahmed, M. El-Sabbah, S. M. El-Bahy, A. Fahmy, Influence of pH values on the electrochemical performance of low carbon steel coated by plasma thin SiO_xC_y films. *Arab. J. Chem.* **14**, 103391 (2021).
84. P.-R. Cha, H.-S. Han, G.-F. Yang, Y.-C. Kim, K.-H. Hong, S.-C. Lee, J.-Y. Jung, J.-P. Ahn, Y.-Y. Kim, S.-Y. Cho, J. Y. Byun, K.-S. Lee, S.-J. Yang, H.-K. Seok, Biodegradability engineering of biodegradable Mg alloys: Tailoring the electrochemical properties and microstructure of constituent phases. *Sci. Rep.* **3**, 2367 (2013).
85. M. A. Khalili, E. Tamjid, Controlled biodegradation of magnesium alloy in physiological environment by metal organic framework nanocomposite coatings. *Sci. Rep.* **11**, 8645 (2021).
86. C. Li, C. Guo, V. Fitzpatrick, A. Ibrahim, M. J. Zwierstra, P. Hanna, A. Lechtig, A. Nazarian, S. J. Lin, D. L. Kaplan, Design of biodegradable, implantable devices towards clinical translation. *Nat. Rev. Mater.* **5**, 61–81 (2020).
87. P. P. Mueller, S. Arnold, M. Badar, D. Bormann, F.-W. Bach, A. Drynda, A. Meyer-Lindenberg, H. Hauser, M. Peuster, Histological and molecular evaluation of iron as degradable medical implant material in a murine animal model. *J. Biomed. Mater. Res. A* **100A**, 2881–2889 (2012).
88. U. Schwertmann, Solubility and dissolution of iron oxides. *Plant Soil* **130**, 1–25 (1991).
89. A. Francis, Y. Yang, S. Virtanen, A. R. Boccaccini, Iron and iron-based alloys for temporary cardiovascular applications. *J. Mater. Sci. Mater. Med.* **26**, 138 (2015).
90. L. Yin, X. Huang, H. Xu, Y. Zhang, J. Lam, J. Cheng, J. A. Rogers, Materials, designs, and operational characteristics for fully biodegradable primary batteries. *Adv. Mater.* **26**, 3879–3884 (2014).
91. R. C. Lucacel, O. Ponta, E. Licarete, T. Radu, V. Simon, Synthesis, structure, bioactivity and biocompatibility of melt-derived P_2O_5-CaO-B_2O_3-K_2O-MoO_3 glasses. *J. Non Cryst. Solids* **439**, 67–73 (2016).
92. M. Peuster, C. Fink, P. Wohlsein, M. Bruegmann, A. Günther, V. Kaese, M. Niemeyer, H. Haferkamp, C. v. Schnakenburg, Degradation of tungsten coils implanted into the subclavian artery of New Zealand white rabbits is not associated with local or systemic toxicity. *Biomaterials* **24**, 393–399 (2003).
93. M. Peuster, C. Fink, C. von Schnakenburg, Biocompatibility of corroding tungsten coils: In vitro assessment of degradation kinetics and cytotoxicity on human cells. *Biomaterials* **24**, 4057–4061 (2003).
94. S. Kanokpanont, S. Damrongsakkul, J. Ratanavaraporn, P. Aramwit, Physico-chemical properties and efficacy of silk fibroin fabric coated with different waxes as wound dressing. *Int. J. Biol. Macromol.* **55**, 88–97 (2013).
95. H. C. Chen, C.-H. Kuo, H. H. Chen, Y.-C. Liu, C. J. Shieh, Optimization of enzymatic synthesis of Cetyl 2-ethylhexanoate by Novozym® 435. *J. Am. Oil Chem. Soc.* **88**, 1917–1923 (2011).
96. C. Redlich, A. Schauer, J. Scheibler, G. Poehle, P. Barthel, A. Maennel, V. Adams, T. Weissgaerber, A. Linke, P. Quadbeck, In vitro degradation behavior and biocompatibility of bioresorbable molybdenum. *Metals* **11**, 761 (2021).
97. L. E. Bevers, P.-L. Hagedoorn, W. R. Hagen, The bioinorganic chemistry of tungsten. *Coord. Chem. Rev.* **253**, 269–290 (2009).
98. D. G. Barceloux, Molybdenum. *J. Toxicol. Clin. Toxicol.* **37**, 231–237 (1999).
99. P. Trumbo, A. A. Yates, S. Schlicker, M. Poos, Dietary reference intakes. *J. Am. Dietetic Assoc.* **101**, 294–301 (2001).
100. N. Strigul, Does speciation matter for tungsten ecotoxicology? *Ecotoxicol. Environ. Saf.* **73**, 1099–1113 (2010).
101. H.-S. Han, S. Loffredo, I. Jun, J. Edwards, Y.-C. Kim, H.-K. Seok, F. Witte, D. Mantovani, S. Glyn-Jones, Current status and outlook on the clinical translation of biodegradable metals. *Mater. Today* **23**, 57–71 (2019).
102. K. J. Yu, D. Kuzum, S.-W. Hwang, B. H. Kim, H. Juul, N. H. Kim, S. M. Won, K. Chiang, M. Trumpis, A. G. Richardson, H. Cheng, H. Fang, M. Thompson, H. Bink, D. Talos, K. J. Seo, H. N. Lee, S.-K. Kang, J.-H. Kim, J. Y. Lee, Y. Huang, F. E. Jensen, M. A. Dichter, T. H. Lucas, J. Viventi, B. Litt, J. A. Rogers, Bioresorbable silicon electronics for transient spatiotemporal mapping of electrical activity from the cerebral cortex. *Nat. Mater.* **15**, 782–791 (2016).
103. S.-K. Kang, R. K. J. Murphy, S.-W. Hwang, S. M. Lee, D. V. Harburg, N. A. Krueger, J. Shin, P. Gamble, H. Cheng, S. Yu, Z. Liu, J. G. McCall, M. Stephen, H. Ying, J. Kim, G. Park,

Downloaded from https://www.science.org on October 16, 2026

R. C. Webb, C. H. Lee, S. Chung, D. S. Wie, A. D. Gujar, B. Vemulapalli, A. H. Kim, K.-M. Lee, J. Cheng, Y. Huang, S. H. Lee, P. V. Braun, W. Z. Ray, J. A. Rogers, Bioresorbable silicon electronic sensors for the brain. *Nature* **530**, 71–76 (2016).
104. C. Redlich, P. Quadbeck, M. Thieme, B. Kieback, Molybdenum – A biodegradable implant material for structural applications? *Acta Biomater.* **104**, 241–251 (2020).
105. P. A. Nikolaychuk, A. G. Tyurin, The revised pourbaix diagram for molybdenum. *Butlerov Commun.* **24**, 101–105 (2011).
106. G. Schwarz, R. R. Mendel, M. W. Ribbe, Molybdenum cofactors, enzymes and pathways. *Nature* **460**, 839–847 (2009).
107. J. W. Johnson, C. H. Chi, C. K. Chen, W. J. James, The anodic dissolution of molybdenum. *Corrosion* **26**, 238–242 (1970).
108. M. Petrova, M. Bojinov, S. Zanna, P. Marcus, Mechanism of anodic oxidation of molybdenum in nearly-neutral electrolytes studied by electrochemical impedance spectroscopy and X-ray photoelectron spectroscopy. *Electrochim. Acta* **56**, 7899–7906 (2011).
109. J. R. Turnlund, W. R. Keyes, G. L. Peiffer, G. Chiang, Molybdenum absorption, excretion, and retention studied with stable isotopes in young men during depletion and repletion. *Am. J. Clin. Nutr.* **61**, 1102–1109 (1995).
110. A. Yamamoto, R. Honma, M. Sumita, Cytotoxicity evaluation of 43 metal salts using murine fibroblasts and osteoblastic cells. *J. Biomed. Mater. Res.* **39**, 331–340 (1998).
111. O. Ponta, R. Ciceo-Lucacel, A. Vulpoi, T. Radu, S. Simon, Molybdenum effect on the structure of SiO_2–CaO–P_2O_5 bioactive xerogels and on their interface processes with simulated biofluids. *J. Biomed. Mater. Res. A* **102**, 3177–3185 (2014).
112. J. C. Middleton, A. J. Tipton, Synthetic biodegradable polymers as orthopedic devices. *Biomaterials* **21**, 2335–2346 (2000).
113. L. S. Nair, C. T. Laurencin, Biodegradable polymers as biomaterials. *Prog. Polym. Sci.* **32**, 762–798 (2007).
114. P. Ritter, G. Z. Duray, S. Zhang, C. Narasimhan, K. Soejima, R. Omar, V. Laager, K. Stromberg, E. Williams, D. Reynolds, Micra Transcatheter Pacing Study Group, The rationale and design of the Micra Transcatheter Pacing Study: Safety and efficacy of a novel miniaturized pacemaker. *Europace* **17**, 807–813 (2015).
115. V. Y. Reddy, R. E. Knops, J. Sperzel, M. A. Miller, J. Petru, J. Simon, L. Sediva, J. R. de Groot, F. V. Y. Tjong, P. Jacobson, A. Ostrosff, S. R. Dukkipati, J. S. Koruth, A. A. M. Wilde, J. Kautzner, P. Neuzil, Permanent leadless cardiac pacing. *Circulation* **129**, 1466–1471 (2014).

Acknowledgments: We acknowledge the collaborative platform provided by the Phase III "Exploration Program for Innovation Capacity Development in the Capital Medical and Health Field." **Funding:** This work was supported by the National Natural Science Foundation (grant number 22479016 to D.W.). **Author contributions:** D.W. and F.Y. initiated and conceived the magnetically gated pacing concept. D.W., W.S., and Z.L.W. supervised the whole project. F.Y., Y.T., and W.S. designed the studies and analysed the results. F.Y., L.Y., P.P., H.Q., and Y.D. fabricated and characterized the devices. Y.T., W.S., Ha.L., and Y.W. conducted animal surgeries. F.Y., Y.T., and W.S. performed in vivo cardiac pacing experiments. F.Y. and D.W. developed proof-of-concept closed-loop system. E.Z., Ho.L., and T.-L.R. performed computational simulations. Z.Y. and A.Z. developed the dedicated microcontroller-based testing platform. F.Y. and L.Y. developed and synthesized the hydrogels. F.Y., Y.T., and W.S. evaluated the biocompatibility. F.Y., Y.T., Ha.L., Y.W., W.S., and D.W. discussed and interpreted the data. D.W. and F.Y. prepared figures and wrote the paper. In addition, P.P., H.Q., and Y.D. assisted with the preparation of figures. F.Y., T.-L.R., W.S., Z.L.W., and D.W. revised the paper. **Competing interests:** The authors declare they have no competing interests. **Data, code, and materials availability:** All data and code needed to evaluate and reproduce the results in the paper are present in the paper and/or the Supplementary Materials. This study did not generate any new materials.

Submitted 2 April 2026
Accepted 10 September 2026
Published 16 October 2026
10.1126/sciadv.aeh6700

Downloaded from https://www.science.org on October 16, 2026

ScienceAdvances

Magnetically gated millimeter-scale capsule power system for leadless electrotherapy

Feiyao Yang, Yu Tian, Enyi Zhang, Lixue Yang, Ziyue You, Puguang Peng, Han Qian, Yan Du, Haiwei Li, Yongquan Wu, Houfang Liu, Anfu Zhou, Tian-Ling Ren, Weiping Sun, Zhong Lin Wang, and Di Wei

Sci. Adv. **12** (42), eaeh6700. DOI: 10.1126/sciadv.aeh6700

View the article online
https://www.science.org/doi/10.1126/sciadv.aeh6700
Permissions
https://www.science.org/help/reprints-and-permissions

Downloaded from https://www.science.org on October 16, 2026

Use of this article is subject to the Terms of service

Science Advances (ISSN 2375-2548) is published by the American Association for the Advancement of Science. 1200 New York Avenue NW, Washington, DC 20005. The title *Science Advances* is a registered trademark of AAAS.

Copyright © 2026 The Authors, some rights reserved; exclusive licensee American Association for the Advancement of Science. No claim to original U.S. Government Works. Distributed under a Creative Commons Attribution NonCommercial License 4.0 (CC BY-NC).